PCCP

PAPER

View Article Online
View Journal | View Issue

Cite this: *Phys. Chem. Chem. Phys.*, 2025, **27**, 1534

Suboxides and subselenides: intermediate reaction products to form Ga_2O_3, Ga_2Se_3, In_2O_3, In_2Se_3, SnO_2, and $SnSe_2$ during molecular-beam epitaxy

Patrick Vogt, *[a] Shun-Li Shang [b] and Zi-Kui Liu [b]

Received 25th April 2024,
Accepted 18th November 2024

DOI: 10.1039/d4cp01702a

rsc.li/pccp

The molecular-beam epitaxial (MBE) growth of III-O and IV-O materials (*e.g.*, Ga_2O_3, In_2O_3, and SnO_2) is known to be reaction-limited by complex 2-step kinetics and the desorption of volatile suboxides (*e.g.*, Ga_2O, In_2O, SnO). We find that the different surface reactivities of suboxides and respective elements (*e.g.*, Ga, In, Sn) with active oxygen define the film-growth-windows (FGWs) and suboxide-formation-windows (SFWs) of III-O and IV-O materials, respectively. To generalize, we provide elementary reaction pathways and respective Gibbs energies to form binary III-O, III-Se, IV-O, and IV-Se ground-states as well as their subcompounds during their MBE growth. We apply the 2-step kinetics model established for oxides to identify the subselenide-limited growth of Ga_2Se_3 as the specific example for III-Se materials. Our kinetic and thermodynamic conclusions suggest subcompound-limited growth may be an inherent property for the growth of III–VI and IV–VI thin films by MBE and related epitaxial growth techniques.

I. Introduction

In 'classical' molecular-beam epitaxy (MBE) elemental cations react directly with reactive anions to form the intended compound on a heated single-crystalline substrate.[1–4] This is because the MBE growth of III–V and II–VI materials is governed by simple 1-step reaction kinetics.[3,5–10] This basic surface physics and reaction kinetics has been one of the prerequisites to controllably synthesize functional thin films at the highest crystalline level,[11,12] for example, enabling the discovery of novel physics at thin film interfaces.[13]

On the other hand, the MBE growth of III-O and IV-O materials is more complex and determined by complex 2-step reaction kinetics and limited by the formation of volatile suboxides (*e.g.*, Ga_2O, In_2O, and SnO).[14–19] These complex surface reactions kinetically prohibit the growth of functional III-O and IV-O thin films in their adsorption-controlled growth regimes.[20,21]

Based on the common valences between III–VI or IV–VI materials, it is conceivable that the growth kinetics of III-Se and IV-Se is similar to that of III-O and IV-O compounds. Previous MBE studies on Ga_2Se_3 and In_2Se_3 indicate their growth to be limited by the formation of their subselenides Ga_2Se and In_2 Se, respectively[22–24] —similar to Ga_2O_3 and In_2O_3 being limited by the formation of their suboxides Ga_2O and In_2O. However, the underlying reaction kinetics that form III-Se and IV-Se thin films remains elusive and the lack of microscopically understanding their reaction pathways hinders the full exploration of growth conditions and their impact on the phase formation and material properties of functional selenide-based thin films.[25–29]

In this paper, we start with identifying the surface reactivities (η_M) of elemental metal (with M = Ga, In, and Sn) as well as the surface reactivities (η_S) of molecular suboxides (with S = Ga_2O, In_2O, and SnO) reacting with oxygen, and find that $\eta_M \geq \eta_S$. As a consequence of $\eta_M \geq \eta_S$, the film-growth-windows (FGWs) of III-O and IV-O materials fundamentally change upon growth conditions; as we explicitly demonstrate by the example of Ga_2O_3. We next model the growth of Ga_2Se_3 by complex 2-step kinetics and obtain a similar result as established for Ga_2O_3 growth.[30] To strengthen our model results, we provide elemental reaction pathways and thermodynamic calculations for the Ga_2O_3, Ga_2Se_3, In_2O_3, In_2Se_3, SnO_2, and $SnSe_2$ growth systems. In all cases, we obtain that suboxides and subselenides are the cationic-like *volatile* species in each material system and we propose that subcompounds (*e.g.*, suboxides and subselenides) are the intermediate and rate-limiting reaction products for III–VI and IV–VI MBE growth, in general.

II. Suboxide-formation-window (SFW) *versus* film-growth-window (FGW)

To understand the origin of different surface reactivities between adsorbed metals (*e.g.*, Ga) and formed suboxides (*e.g.*, Ga_2O)

[a] *Institute of Solid-State Physics, University of Bremen, Otto-Hahn-Allee 1, Bremen, 28359, Germany. E-mail: p.vogt@fkf.mpg.de*
[b] *Department of Materials Science and Engineering, Pennsylvania State University, University Park, Pennsylvania 16802, USA*

reacting with oxygen, Fig. 1(a)–(g) collect published growth rate (Γ) data of Ga_2O_3,[15,31–33] In_2O_3,[31] and SnO_2,[14] normalized by their respective nominal oxygen flux, ϕ_O. It depicts the fundamental Γ evolutions depending on the metal-to-oxygen flux ratio, $R = \phi_M/\phi_O$, at given growth temperature, T_G, and metal flux, ϕ_M.

We start with the observed Γ plateaus: the solid lines in Fig. 1(a)–(g) reflect the film-growth-windows (FGWs) of Ga_2O_3, In_2O_3, and SnO_2, obtained by experimental data (shown by the open symbols). At elevated T_G, a Γ plateau emerges and widens with increasing T_G. We define the value of Γ at the plateau as the value of maximum cation incorporation into the thin film at given T_G. Based on the 2-step kinetics of these materials,[20,31] this Γ value thus gives the maximum available oxygen reservoir for suboxide-to-oxide formation (S-to-O). This also defines the 2nd reaction step to form the oxides Ga_2O_3, In_2O_3, and SnO_2, *via* the reactions:[31]

$$Ga_2O(a) + 2O(a) \xrightarrow{K} Ga_2O_3(s) \quad (1)$$

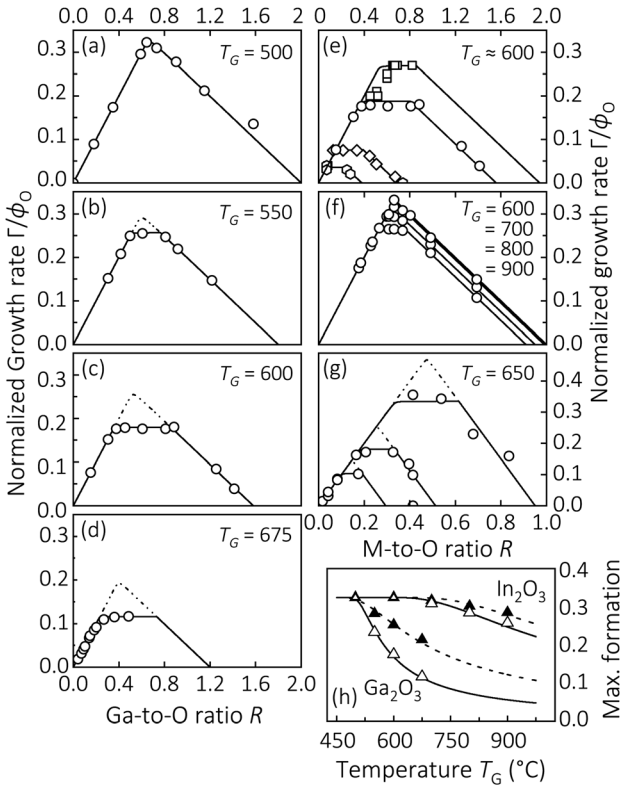

Fig. 1 (a)–(d) Γ normalized by ϕ_O (Γ/ϕ_O) of β-Ga_2O_3 ($\bar{2}01$) as a function of the Ga-to-O ratio ($R = \phi_{Ga}/\phi_O$), measured at different T_G. Data is taken from ref. 31. (e) Γ/ϕ_O as a function of R of β-Ga_2O_3(010) [squares], β-Ga_2O_3($\bar{2}01$) [discs, same data as shown in panel (c)], β-Ga_2O_3(001) [diamonds], and β-Ga_2O_3(100) [hexagons]. Data is taken from ref. 15 and 31–33. (f) Γ/ϕ_O of bixbiyte In_2O_3(111) as a function of the In-to-O ratio ($R = \phi_{In}/\phi_O$), measured at different T_G. Data is taken from ref. 17. (g) Γ/ϕ_O of SnO_2(101) as a function of the Sn-to-O flux ratio ($R = \phi_{Sn}/\phi_O$), obtained at different ϕ_O. Data is taken from ref. 14. (h) Growth-system-dependent maximum M-to-S formation (solid triangles) [eqn (4)–(6)] and maximum S-to-O formation (*i.e.*, the maximum Γ, open triangles) [eqn (1)–(3)] as a function of T_G. Symbols represent experimental data, solid and dotted lines are numeric models[18,31] serving as guides to the eye.

$$In_2O(a) + 2O(a) \xrightarrow{K} In_2O_3(s) \quad (2)$$

$$SnO(a) + O(a) \xrightarrow{K} SnO_2(s), \quad (3)$$

with reaction rate constant, K. Adsorbate and solid phases are denoted as a and s, respectively.

To explain the origin of the Γ plateau as well as the onset of the Γ decrease, we now define the suboxide-reaction-window (SRW) for metal-to-suboxide formation (M-to-S). This defines the 1st reaction step to form Ga_2O_3, In_2O_3, and SnO_2 through forming the suboxides Ga_2O, In_2O, and SnO, respectively, *via* the reactions:[31]

$$2Ga(a) + O(a) \xrightarrow{\kappa} Ga_2O(a, g) \quad (4)$$

$$2In(a) + O(a) \xrightarrow{\kappa} In_2O(a, g) \quad (5)$$

$$Sn(a) + O(a) \xrightarrow{\kappa} SnO(a, g), \quad (6)$$

with reaction rate constant, κ. The gaseous phase is denoted as g and refers to the volatility of suboxides during growth. The SRW is indicated by the dotted lines in Fig. 1(b)–(e) and (g) and obtained by extending the Γ evolutions from extending the M-rich growth regime (the *decreasing* Γ with ϕ_M) as well as the O-rich regime (the *increasing* Γ with ϕ_M) until both lines intersect—always forming a triangular shape. The suboxides formed during the 1st reaction step, eqn (4)–(6), can be further oxidized to the solid compound through a 2nd reaction step, eqn (1)–(3), or desorb from the growth surface and limit Γ. As a result, the SRW for M-to-S formation is equal to or wider than the FGW for S-to-O formation, *i.e.*, $\kappa \geq K$, depending on T_G. To illustrate their quantitative differences, the maximum (normalized) formation rates of Ga_2O and Ga_2O_3 as well as of In_2O and In_2O_3 are plotted as a function of T_G in Fig. 1(h). A detailed explanation of this effect is given in Fig. 2. The maximum suboxide formation is defined as the peak value of the SRWs, seen by dotted lines in Fig. 1(b)–(d) and (g). In the case of SnO_2, we obtain the suboxide formation is about 1.4Γ for all ϕ_O at T_G = 650 °C. Overall, the reactivity of Sn > In > Ga with O is higher than the one of SnO > In_2O > Ga_2O with O, respectively. This feature can also be referred to the different vapor pressures and surface reactivities of the respective elements and suboxides.[16,18,34–38]

Fig. 1(f) and (g) depict the Γ evolutions of In_2O_3 and SnO_2, respectively, as a function of R, showing qualitatively the same kinetic behaviour as observed for Ga_2O_3. The quantitative differences in Γ between III-O and IV-O materials arise from the different group III-O and IV-O suboxide stoichiometries as well as their different surface reactivities.[16,37]

Note, for the sake of simplicity, reactions (1)–(6) are selected as specific examples but may be generalized for other III-O and IV-O materials. For example, the knowledge of the 2-step reaction kinetics was used to form Al_2O_3,[40] rutile GeO_2,[41] or amorphous GeO_2[42] *via* the formation of their suboxides Al_2O and GeO, respectively. We further note that a 'direct reaction' to form the solid-state compound, *e.g.*, *via* 2Ga + 3O → Ga_2O_3, can be kinetically excluded. This assumption is reasonable as the formation of complex compounds can be (usually) described by

a set of elementary reactions rather than by *non*-elementary reactions.[43] In other words, forming the oxide thin film *via* a set of multiple elementary surface reactions *via* a suboxide formation step is kinetically preferred over a single *non*-elemental surface reaction step. As the suboxide itself may also undergo a multi-step reaction pathway, we propose a general reaction scheme to form binary III–VI and IV–VI materials and sketch their possible reaction pathways in Fig. 5 (see below).

A. Surface-orientation Γ dependence of Ga_2O_3

Fig. 1(e) shows the comparison of β-Ga_2O_3 FGWs for different surface orientations of β-Ga_2O_3(010), β-Ga_2O_3($\bar{2}$01), β-Ga_2O_3(001), and β-Ga_2O_3(100) as a function of R, at otherwise similar growth conditions.[15,17,32,33] At given $T_G \approx 600$ °C,[15,31–33] the orientation dependence of Γ on the (hkl) plane, $\Gamma_{(hkl)}$, for β-Ga_2O_3 is quantified as

$$\Gamma_{(010)} \approx 1.5\Gamma_{(\bar{2}01)} \approx 3.7\Gamma_{(001)} \approx 7.7\Gamma_{(100)}. \quad (7)$$

Note this quantification depends on the adsorption and desorption kinetics of Ga_2O on the respective β-Ga_2O_3 (hkl) growth plane and strongly depends on T_G.[15,30,44] For example, at T_G = 500 °C the relation $\Gamma_{(010)} \approx 2.1\Gamma_{(\bar{2}01)}$ was observed,[20] suggesting a different functional dependence of sticking coefficients on the respective Ga_2O_3 growth surface. We thus qualitatively propose, the orientation-dependent Γ evolution of Ga_2O_3 can be explained by an interplay of the corresponding orientation-dependent O sticking coefficients (σ) and suboxide surface reactivities η_S, leading to:

$$\Gamma_{(010)} > \Gamma_{(\bar{2}01)} > \Gamma_{(001)} > \Gamma_{(100)}. \quad (8)$$

A similar orientation-dependent Γ of β-Ga_2O_3 in binary Ga–O and Ga_2O–O systems is reported in ref. 18, 33 and 44.

B. Suboxides limiting the growth domain of III-O compounds

For all compounds, we find that SRW ≥ FGW, thus, the physical origin of changing FGWs and emerging Γ plateaus can now explained.

Fig. 2(a) sketches the Γ evolutions of Ga_2O_3 ($\bar{2}$01) at T_G = 500 °C (the gray shaded area) and T_G = 600 °C (the purple shaded area), see also Fig. 1(a) and (c). Four regimes are indicated: (i) the O-rich growth regime, *i.e.*, the *increasing* Γ with increasing Ga flux, ϕ_{Ga}. In this regime, enough O adsorbates are available to fully oxidize all adsorbed Ga *via* the consecutive reaction Ga → Ga_2O → Ga_2O_3 [reactions (4) and (1)]. (ii) The 'pseudo' O-rich growth regime identified by the width of the Γ plateau, λ. Here, enough O adsorbates are available to oxidize all adsorbed Ga to its suboxide *via* Ga → Ga_2O [reaction (4)] but not enough O is available to oxidize all formed suboxides to its solid-state compound *via* Ga_2O → Ga_2O_3 [reaction (1)]—due to thermally-induced suboxide desorption. In other words, the Γ plateau emerges once the formed Ga_2O adsorbate density exceeds the O adsorbate density available for reaction Ga_2O → Ga_2O_3 [reaction (1)].[21] (iii) The Ga-rich growth regime identified by the *decreasing* Γ with ϕ_{Ga} and its width, ω. Here, not enough O is available to oxidize all remaining suboxides to its solid-state compound *via* Ga_2O → Ga_2O_3 [reaction (1)]. Now, this is due to an O-deficient-induced suboxide desorption mechanism—in addition to the thermally-induced suboxide desorption identified for regime (ii). (iv) The *no*-growth regime where Ga_2O_3 growth ceases for $R \geq R_m$. Here, not enough O is available to oxidize Ga → Ga_2O [reaction (4)] and reaction (1) becomes kinetically *forbidden* as all available O is consumed in reaction (4).

We next answer the question: Why does Γ start to decrease at R^o [see Fig. 2(a)] and regime (iii) is entered? Each leaving

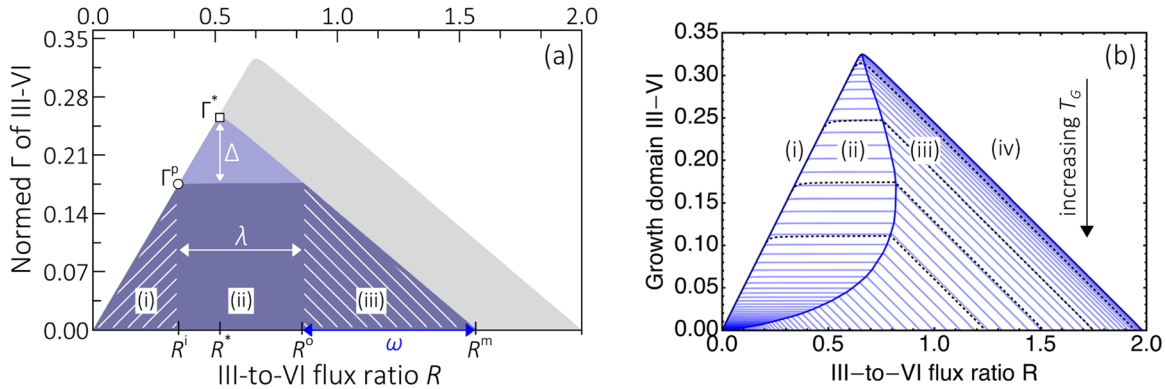

Fig. 2 Γ evolutions for III-O compounds, explicitly drawn for Ga_2O_3. Four distinct growth regimes (i)–(iv) are identified (details provided in the text). (a) The gray and purple areas reflect the modelled film-growth-windows (FGWs) for Ga_2O_3 based on the data obtained at T_G = 500 °C [Fig. 1(a)] and T_G = 600 °C [Fig. 1(c)], respectively. The difference (Δ) between SFW and FGW for Ga-to-Ga_2O formation [eqn (4)] and Ga_2O-to-Ga_2O_3 formation [eqn (1)] is drawn as the pale purple area at T_G = 600 °C. At T_G = 500 °C this difference is zero, *i.e.*, Δ = 0. The length of the Γ plateau is given by λ [regime (ii)] and the width of regime (iii) is defined as ω. All parameters shown here are collected in Table 1. (b) FGWs of Ga_2O_3 as a function of R modelled for 400 °C ≤ T_G ≤ 1200 °C (the pale blue lines), using a numerical approach based on the models given in ref. 18 and 39. At low T_G = 400 °C, the triangular shape defines the maximum accessible $\eta_M = \eta_S \Rightarrow$ SRF = FGW (the dark blue line) divided in regimes (i), (iii), and (iv). With increasing T_G, regime (ii) emerges and the 'shape' of the FGW fundamentally changes to a trapezoidal shape due to $\eta_M > \eta_S \Rightarrow$ SRF > FGW (the dark blue line in the center). The fact that SRF ≥ FGW, changes λ, Δ, and ω, depending on T_G. As a consequence, regime (iii) becomes narrower until it vanishes at high T_G. The black dashed lines correspond to the solid black model lines in Fig. 1(a)–(d) and serve as a guide to the eye.

Ga_2O that cannot be oxidized removes 2 × Ga but only 1 × O from the growth front, producing a more O-rich Ga-to-O surface ratio than expected from the nominally supplied ϕ_{Ga} and ϕ_O. Nevertheless, for $R > R^o$, ϕ_{Ga} and resulting Ga adsorbate density exceed a critical value, resulting in a Ga-rich growth surface and thus regime (iii) is entered. In this regime, not enough O is available to oxidize all formed Ga_2O that have remained on the growth surface (*i.e.*, Ga_2O molecules that have not desorbed), and Γ decreases due to the O-surface-deficiency-induced suboxide desorption. As specific example, all parameters and values for Ga_2O_3 are indicated in Fig. 2(a) and collected in Table 1, which, in turn, are extracted from the data plotted in Fig. 1(a)–(d). After considering all desorbing species, it is found that the Ga_2O_3 growth surface becomes stoichiometric once

$$\frac{\phi_{Ga}}{\phi_O} \geq \frac{2\Gamma^p}{\frac{1}{2}(3R^* - \lambda)} = \frac{n_{Ga}}{n_O} = \frac{x}{y}, \tag{9}$$

see Fig. 2 and Table 1.

The above findings have fundamental consequences for the Γ evolution of III–VI and IV–VI compounds. For example, λ increases and ω decreases with increasing T_G because of the enhanced thermally-induced suboxide desorption. As a result, the 'shape' of the accessible FGW changes upon growth conditions. Based on the data plotted in Fig. 1(a)–(d), Fig. 2(b) now depicts such an Γ evolution as a function of R and different T_G (here of Ga_2O_3).

At low T_G, the triangular shape of the modeled Γ defines the maximum possible FGW for these materials. With increasing T_G, the Γ plateau emerges and the growth domain becomes trapezoidal and narrows until growth eventually ceases. This finding reveals that the growth of Ga_2O_3 in the Ga-rich regime and elevated T_G is hardly possible, associated with extremely slow Γ. Nevertheless, these growth conditions are desired to improve the crystallographic and transport properties of Ga_2O_3 grown by conventional MBE.[28] The same argument holds for In_2O_3, for example.

A solution to overcome these intrinsic and detrimental growth limits for group III and group IV oxides is the use of recent advances in their thin film synthesis, such as *suboxide* MBE (*S*-MBE),[20,21,45] metal-exchange catalysis (MEXCAT)[18,37] with metal-oxide-catalyzed epitaxy (MOCATAXY),[17,46] thermal laser epitaxy (TLE),[40] or hybrid MBE (*h*MBE).[47,48]

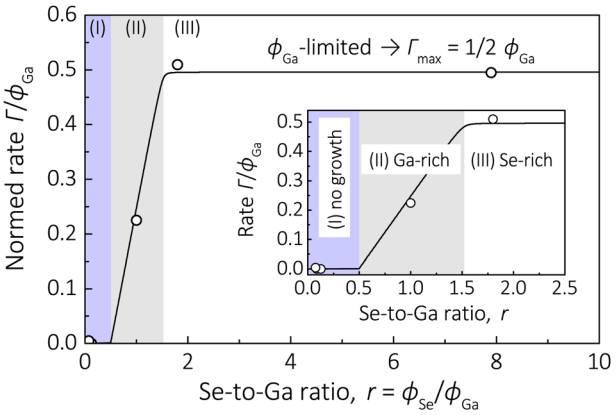

Fig. 3 Normalized Γ/ϕ_{Ga} of α-Ga_2Se_3 as a function of the Se-to-Ga flux ratio, $\phi_{Se}/\phi_{Ga} = r$. Data is taken from ref. 22, Ga and Se densities in α-Ga_2Se_3[49] are used to convert ϕ_{Ga}, ϕ_{Se}, and Γ into $nm^{-2}\ s^{-1}$. The solid black line is the application of the 2-step model to the experimental data. The data and model shown in the main graph and the inset are complementary but displayed for the sake of readability. In the Se-rich rich regime, Γ is maximized and limited by the supplied ϕ_{Ga}. Note, the horizontal axis in this graph is swapped when compared to the horizontal axes in Fig. 1.

These findings can also be transferred to IV-O materials, *e.g.*, SnO_2. In contrast to the 'asymmetric' Γ plateau observed for III-O materials (Fig. 2), the Γ plateau observed for IV-O materials is 'symmetric' as plotted for SnO_2 in Fig. 1(g). The occurrence of an asymmetric Γ plateau (III–VI) or symmetric Γ plateau (IV–VI) can be explained by the different stoichiometries of III-O and IV-O suboxides. For example, during the growth of SnO_2 the desorption of SnO removes 1 × Sn and 1 × O, resulting in the observed symmetric Γ plateau. In contrast to SnO_2, during the growth of Ga_2O_3 the desorption of Ga_2O removes 2 × Ga and 1 × O, resulting in the observed asymmetric Γ plateau. Another quantitative consequence of the different suboxide stoichiometries is the differently observed slopes in their M-rich regimes for III-O and IV-O materials with

$$\left(\frac{\partial\Gamma_{III\text{-}O}}{\partial R}\right)_{M\text{-rich}} = -\frac{1}{2}$$
$$\left(\frac{\partial\Gamma_{IV\text{-}O}}{\partial R}\right)_{M\text{-rich}} = -1, \tag{10}$$

respectively. For example, see Fig. 1(a) for III-O and Fig. 1(g) for IV-O materials.

Table 1 Stoichiometric M-to-O flux ratio, R^*. Maximum suboxide formation rate, Γ^*, for Ga-to-Ga_2O oxidation. The growth rate value at the plateau, Γ^p. Maximum flux ratio where Ga_2O_3 growth is possible, R^m. The flux ratio at the beginning of the plateau, R^i (with 'i' for in). The flux ratio at the end of the plateau, R^o (with 'o' for out). The maximum Ga adsorbates, n_{Ga}, and the maximum O adsorbates, n_O. The difference Δ between the Ga_2O SRW and the Ga_2O_3 FGW. The length λ of the plateau and the width ω of the Ga-rich regime (ii). Finally, the Ga-to-O adsorbate ratio at the end of the plateau, $n_{Ga}/n_O = x/y$ = constant ≤ ϕ_{Ga}/ϕ_O [see eqn (9)]. Parameters are indicated in Fig. 2(a) and values are extracted from the data shown in Fig. 1(a)–(d). This example may serve as a blueprint for all discussed III–VI and IV–VI materials

T_G (°C)	$R^* = 2\Gamma^* = 1/3R^m$	$R^i = n_{Ga} = 2\Gamma^p$	R^o	$\lambda = R^o - R^i$	$n_O = 1/2(3R^* - \lambda)$	$\Delta = \Gamma^* - \Gamma^p$	$\omega = 3R^* - R^o$	n_{Ga}/n_O
500	2/3	2/3	2/3	0	1	0	4/3	=2/3
550	0.58	0.48	0.79	0.31	0.72	0.05	0.97	≈2/3
600	0.52	0.36	0.85	0.49	0.54	0.08	0.71	≈2/3
675	0.48	0.24	0.97	0.73	0.36	0.12	0.42	≈2/3

III. Subselenide-limited growth of Ga_2Se_3

The formation of suboxides has been experimentally reported[14–16] and identified as the growth-limiting step for III-O and IV-O materials and reaction-rate models describing the complex 2-step kinetics for these materials have been developed.[18,31] We anticipate the same kinetics and models can be applied to other III–VI and IV–VI compounds. Therefore, we now apply the 2-step model to the growth of III-Se materials, explicitly, to the growth of Ga_2Se_3.

Fig. 3 shows the Γ evolution of Ga_2Se_3 as a function of the Se-to-Ga ratio, r. The 2-step model described above for oxides is applied to the data and describes the growth kinetics for Ga_2Se_3 very accurately—indicating its MBE growth is limited by Ga_2Se desorption. A similar Γ-behavior is also reported for the growth of In_2Se_3 by MBE.[23] In ref. 22 and 23, it was speculated that the growth of Ga_2Se_3 and In_2Se_3 ceases in the excess of Ga and In fluxes, respectively, due to the re-evaporation of the Ga and Se compounds. However, the physical origin for the observed Γ evolutions for Ga_2Se_3 and In_2Se_3 remained elusive.[22,23] The black lines in Fig. 3 show numeric model calculations by a subselenide-mediated 2-step model. Three distinct regimes are identified: (I) no growth regime for $0 < r = \phi_{Se}/\phi_{Ga} \leq 1/2$, because all reactive Se is consumed for Ga_2Se formation, *i.e.*, $r = 1/2$ defines the stoichiometric flux ratio for $2Ga + Se \rightarrow Ga_2Se$ formation, *e.g.*, *via* reaction (14). (II) The Ga-rich regime is entered for $1/2 < r \leq 3/2$, because not enough reactive Se is available to convert $Ga_2Se \rightarrow Ga_2Se_3$, *e.g.*, *via* reaction (15). The stoichiometric flux ratio for Ga_2Se_3 formation is thus $r = 3/2$. (III) For $r > 3/2$ the Se-rich flux regime is entered and enough reactive Se is available to selenize $Ga \rightarrow Ga_2Se \rightarrow Ga_2Se_3$. Γ is now limited by the supplied ϕ_{Ga}.

Based on the data shown in Fig. 1–3, we can now generalize eqn (10) for III–VI and VI-VI materials for the anion-rich regime (A), plateau regime (P), and cation-rich regime (C) as

$$\left(\frac{\partial\Gamma}{\partial R}\right)_A = y - x, \quad \left(\frac{\partial\Gamma}{\partial R}\right)_P = 0, \quad \left(\frac{\partial\Gamma}{\partial R}\right)_C = 1 - \frac{y}{x}. \qquad (11)$$

IV. Thermodynamic analysis and surface reactions

To support and strengthen our prediction that suboxides and subselenides limit the growth of oxides and selenides, respectively, we now perform thermodynamical calculations. Equilibrium calculations are performed using the SGTE substance database (SSUB5)[50] within the Thermo-Calc software[51] to assess the evaporation behavior of cation-like and anion-like species as a function of temperature of the binary oxides Ga_2O_3, In_2O_3, and SnO_2 and the complementary, binary selenides Ga_2Se_3, In_2Se_3, and $SnSe_2$. The results are plotted in Fig. 4.

For the investigated compounds Ga_2O_3, In_2O_3, SnO_2, In_2Se_3, and $SnSe_2$, we find that the most volatile, cationic-like species at relevant T_G are the suboxides and subselenides Ga_2O, In_2O,

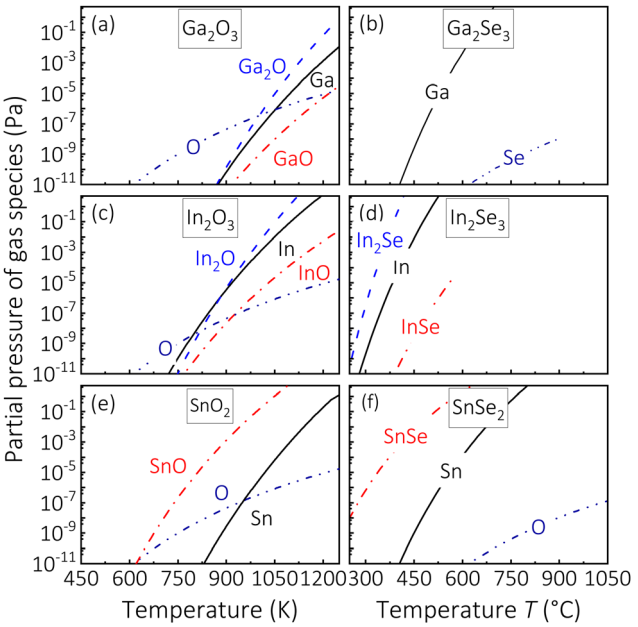

Fig. 4 (a) Calculated partial pressures of the gas species C = Ga, In, Sn, A = O, Se, $C_{y-x}A_{y-x}$ = GaO, InO, InSe, SnO, SnSe [reaction (12)], and C_xA_{y-x} = Ga_2O, In_2O, In_2Se [reactions (13) and (14)].

SnO, In_2Se, and SnSe, respectively, and are in accordance with our kinetics findings that their growth is reaction-limited by subcompound formation and their subsequent desorption. Note, for the Ga_2Se_3 system, the subselenides GaSe and Ga_2Se are missing in the SSUB5 and other thermodynamic databases, thus, we use the kinetic data shown in Fig. 3 to identify that the growth of Ga_2Se_3 is reaction-limited by the subselenide Ga_2Se. This is in agreement with all other investigated growth systems. For example, if Ga was the volatile, cationic species limiting the growth of Ga_2Se_3, Γ would reach a plateau in the Ga-rich regime instead, being similar to the growth kinetics observed for binary III-N compounds.[8] The fact that Γ of Ga_2Se_3 and In_2Se_3 decrease in the Ga-rich and In-rich regimes, respectively, can thus be explained by the desorption of Ga_2Se and In_2Se. We note that the desorption of GaSe and InSe would also explain a decreasing Γ in the cation-rich regimes but with different slopes as given in eqn (11).

In addition, calculated Gibbs energies (ΔG) to form Ga_2Se_3 further strengthen our hypothesis of a 2-step reaction kinetics underlying the formation of III-Se compounds. To unambiguously identify the growth-rate-limiting steps of Ga_2Se_3 and In_2Se_3, *in situ* line-of-sight mass spectroscopy will reveal which subcompound is formed on the respective growth surface.

To microscopically understand the observed and modeled Γ evolutions (Fig. 1–3) and evaporation of suboxides and subselenides, a general reaction scheme for III–VI and IV–VI compounds is proposed in Fig. 5. It depicts a C_xA_y layer (*e.g.*, Ga_2Se_3), impinging cation flux ϕ_c and anion flux ϕ_a, producing the cation (C), anion (A), and subcompound surface populations $C_{y-x}A_{y-x}$ (*e.g.*, GaSe), C_xA_{y-x} (*e.g.*, Ga_2Se), $C_xA_{2(y-x)}$ (*e.g.*, Ga_2Se_2). Stoichiometric coefficients for III–VI and IV–VI materials are $x = 2$ and $y = 3$ as well as $x = 1$ and $y = 2$, respectively. The reaction

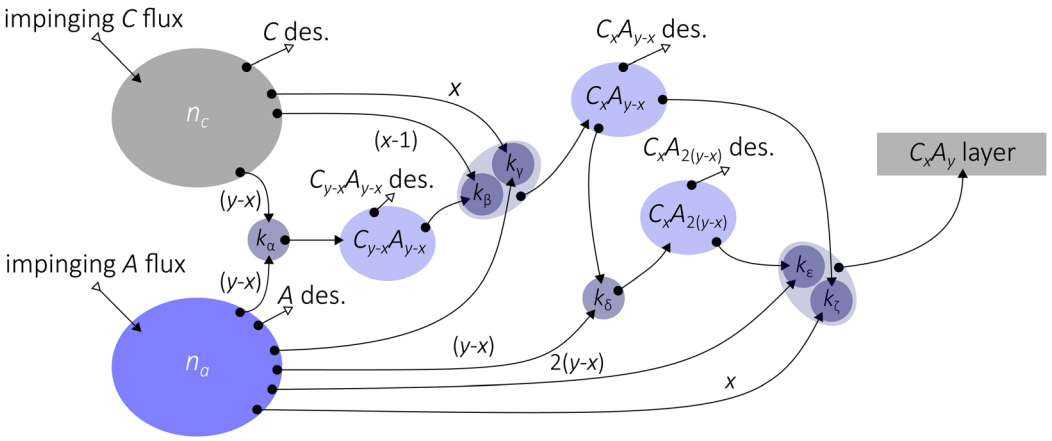

Fig. 5 MBE reaction scheme for binary III–VI and IV–VI materials, showing impinging ϕ_c and ϕ_a, resulting cation n_c, anion n_a, respective subcompound reservoirs, and the final compound C_xA_y. Chemical reactions (12)–(17) are indicated by reaction rate constants k_i.

scheme depicted in Fig. 5 is an extension and refinement of the reaction scheme introduced in ref. 31.

Consecutive reaction pathways to form III-O, III-Se, IV-O, and IV-Se are:

$$(y-x)C(\mathrm{a}) + (y-x)A(\mathrm{a}) \xrightarrow{k_\alpha} C_{y-x}A_{y-x}(\mathrm{a,g}) \quad (12)$$

$$C_{y-x}A_{y-x}(\mathrm{a}) + (x-1)C(\mathrm{a}) \xrightarrow{k_\beta} C_xA_{y-x}(\mathrm{a,g}) \quad (13)$$

$$xC(\mathrm{a}) + (y-x)A(\mathrm{a}) \xrightarrow{k_\gamma} C_xA_{y-x}(\mathrm{a,g}) \quad (14)$$

$$C_xA_{y-x}(\mathrm{a}) + (y-x)A(\mathrm{a}) \xrightarrow{k_\delta} C_xA_{2(y-x)}(\mathrm{a,g}) \quad (15)$$

$$C_xA_{2(y-x)}(\mathrm{a}) + (2x-y)A(\mathrm{a}) \xrightarrow{k_\varepsilon} C_xA_y(\mathrm{s}) \quad (16)$$

$$C_xA_{y-x}(\mathrm{a}) + xA(\mathrm{a}) \xrightarrow{k_\zeta} C_xA_y(\mathrm{s}) \quad (17)$$

with reaction rate constant k_i with $i = \alpha, \beta, \gamma, \delta, \varepsilon, \zeta$. In eqn (13), the relation $y - 1 = x$ is used. Note, for the growth of IV–VI compounds, reactions (13) and (16) are forbidden and reactions (15) and (17) are identical due to their stoichiometric coefficients $x = 1$ and $y = 2$. Consequently, the surface reaction pathways for IV–VI are not as complex as for III–VI compounds.

It has been shown for III-O materials (*e.g.*, Ga_2O_3) and IV-O materials (*e.g.*, SnO_2) that these compounds can be chemically decomposed (etched) by their respective elemental metal (*e.g.*, Ga or Sn) to form its respective suboxide (*e.g.*, GaO, Ga_2O, or SnO)[16] *via* the reactions

$$(y-x)C(\mathrm{a}) + C_xA_y(\mathrm{s}) \xrightarrow{e_\alpha} yC_{y-x}A_{y-x}(\mathrm{a,g}) \quad (18)$$

$$x(y-1)C(\mathrm{a}) + C_xA_y(\mathrm{s}) \xrightarrow{e_\beta} yC_xA_{y-x}(\mathrm{a,g}) \quad (19)$$

with etching rate constants e_α and e_β to form the subcompounds $C_{y-x}A_{y-x}$ (*e.g.*, GaO or GaSe) and C_xA_{y-x} (*e.g.*, Ga_2O or Ga_2Se), respectively. Note, for III-O materials only reaction (19) has been experimentally observed under MBE conditions.[16]

Finally, Fig. 6 plots our calculated ΔG using eqn (20)–(24) as a function of T_G of Ga_2O_3, Ga_2Se_3, In_2O_3, In_2Se_3, SnO_2, and $SnSe_2$ (calculations are given in the Appendix I). We calculated ΔG for

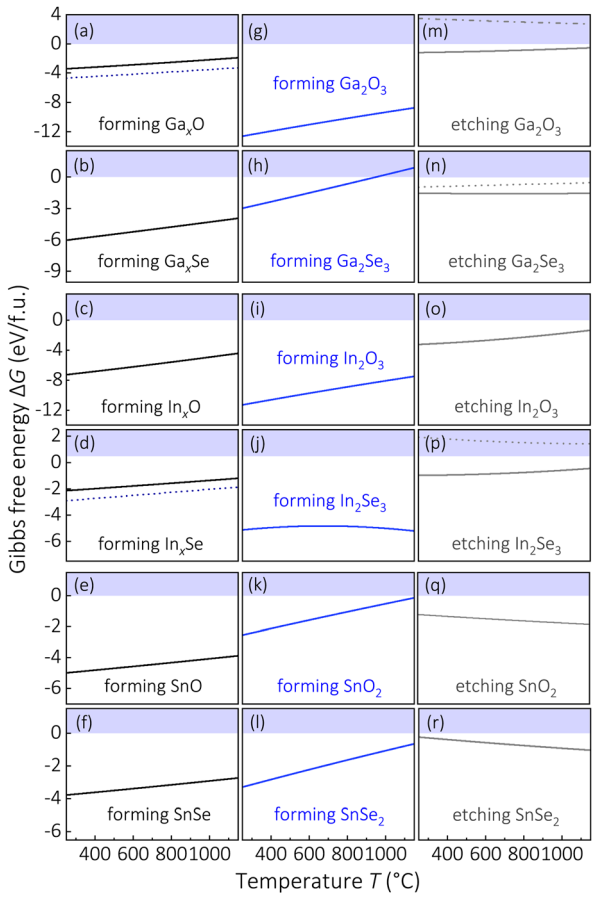

Fig. 6 The Gibbs energy (ΔG) as a function of temperature T. Values of ΔG are in eV per formula unit (f.u.). (a)–(f) ΔG for subcompound formations *via* eqn (12) [black solid lines] and eqn (13) [dark-blue dotted lines]. (g)–(l) ΔG for solid thin film formations *via* eqn (17) [blue solid lines]. (m)–(r) ΔG for thin film etching to form subcompounds *via* eqn (18) [gray dotted lines] and eqn (19) [gray solid lines].

growth and etch reactions (12)–(19) once data were available.[52] For all investigated materials and relevant T_G, the formation of the suboxide and subselenide is thermodynamically feasible. This is in agreement with the observed III-O and IV-O kinetics and we further calculate that III-Se and IV-Se compounds can be chemically decomposed by their elemental metal to form their respective subselenide through reactions (18) and (19). We thus conjecture that the formation of suboxides and subselenides is kinetically and thermodynamically favorable and the rate-limiting step for a wide-range of III-O, III-Se, IV-O, and IV-Se compound materials.

V. Conclusions

We identify by published growth rate (Γ) data of the Ga_2O_3, In_2O_3, and SnO_2 growth systems that the elements Ga, In, and Sn possess a higher reaction efficiency (η_M) with adsorbed O than their corresponding volatile suboxides (η_S) Ga_2O, In_2O, and SnO. We find that $\eta_M \geq \eta_S$ and quantified the fundamental growth domain of III–VI materials whose regimes strongly depend on MBE growth conditions and find that SFW $\geq$ FGW. In particular, we observe a vanishing M-rich growth regime with increasing T_G, leading to off-stoichiometric growth surfaces concerning their initially adsorbed densities of group III and group VI elements.

By combining a 2-step kinetic model to experimental Γ data of Ga_2Se_3 with our thermodynamic analysis and calculations we find the volatile species for the Ga_2Se_3, In_2Se_3, and $SnSe_2$ systems are the subselenides Ga_2Se, In_2Se, and SnSe, respectively. We provide a detailed reaction diagram for the growth of III-O, III-Se, IV-O, and IV-Se materials systems, supported by thermodynamic calculations.

The identified thermodynamic and kinetic feasibility of the proposed 2-step reaction mechanisms for III-Se and IV-Se materials let us conclude that III-Se and IV-Se compounds grow *via* (qualitatively) the same 2-step reaction mechanism—similar to what is established for III-O and IV-O materials.[21,31,38] To unambiguously identify the growth-rate-limiting steps and volatile species of the proposed binary III-O, III-Se, IV-O, and IV-Se growth systems [*e.g.*, eqn (12)–(19)], *in situ* line-of-sight mass spectroscopy will reveal which subcompound is formed on the respective growth surface.

Author contributions

Patrick Vogt: conceptualization (lead), data curation (lead), formal analysis (lead), investigation (lead), methodology (lead), writing original draft (lead). Shun-Li Shang: methodology (equal), data curation (equal), formal analysis (supporting), investigation (supporting), writing original draft (supporting). Zi-Kui Liu: data curation (supporting), investigation (supporting), methodology (supporting), writing original draft (supporting).

Data availability

Data is available upon reasonable request from the corresponding authors.

Conflicts of interest

The authors have no conflicts of interest to declare.

Appendices

Appendix I

Thin film growth *via* MBE takes place under isobaric-isothermal conditions. The change in the Gibbs energy $\Delta G(T)$ at given temperature T is

$$\Delta G(T) = \Delta H(T) - T\Delta S(T), \tag{20}$$

with the change in enthalpy $\Delta H(T)$ and the change in entropy $\Delta S(T)$ determined as

$$\Delta H(T) = \Delta H_0 + \int_{T_0}^{T_G} \mathrm{d}T\, C(T) \tag{21}$$

$$\Delta S(T) = \Delta S_0 + \int_{T_0}^{T_G} \mathrm{d}T \left(\frac{C(T)}{T}\right), \tag{22}$$

respectively. ΔH_0 and ΔS_0 denote the change in ΔH and ΔS at room temperature, T_0 = 295 K. The heat capacity $C(T)$ is calculated as

$$C(T) = a + b\ 10^{-3}T + c\ 10^{6}T^{-2} + d\ 10^{-6}T^{2}. \tag{23}$$

For all discussed species, ΔH_0, ΔS_0, a, b, c, and d are taken from ref. 52. A chemical reaction may occur spontaneously once $\Delta G < 0$. For a given reaction, with reactants R_i and products P_j, it can be determined by the sum of the Gibbs energies of P_j, $\sum_j G_{P_j}$, minus the sum of the Gibbs energies of R_i, $\sum_i G_{R_i}$, *i.e.*

$$\Delta G = \sum_j p_j G_{P_j} - \sum_i r_i G_{R_i}. \tag{24}$$

The stoichiometric coefficients of R_i and P_j are denoted as r_i and p_j, respectively.

Acknowledgements

PV acknowledges the Max Planck Institute for Solid State Research for financial support and Martin Eickhoff and Alexander Karg for fruitful discussions regarding the reaction chemistries of III-O compounds. SLS and ZKL acknowledge the support from Endowed Dorothy Pate Enright Professorship at the Pennsylvania State University.

References

1 J. R. Arthur, *J. Appl. Phys.*, 1968, **39**, 4032, DOI: 10.1063/1.1656901.
2 M. Copel, M. C. Reuter, E. Kaxiras and R. M. Tromp, *Phys. Rev. Lett.*, 1989, **63**, 632, DOI: 10.1103/PhysRevLett.63.632.
3 K. Ploog, *Annu. Rev. Mater. Sci.*, 1982, **12**, 123, DOI: 10.1146/annurev.ms.12.080182.001011.

4 J. Neugebauer, T. K. Zywietz, M. Scheffler, J. E. Northrup, H. Chen and R. M. Feenstra, *Phys. Rev. Lett.*, 2003, **90**, 056101, DOI: 10.1103/PhysRevLett.90.056101.
5 K. Ploog, *Annu. Rev. Mater. Sci.*, 1981, **11**, 171, DOI: 10.1146/annurev.ms.11.080181.001131.
6 H. Riechert, R. Averbeck, A. Graber, M. Schienle, U. Straub and H. Tews, *MRS Online Proc. Libr.*, 1996, **449**, 149–159, DOI: 10.1557/PROC-449-149.
7 E. Calleja, M. A. Sánchez-García, F. J. Sánchez, F. Calle, F. B. Naranjo and E. Muñoz, *et al.*, *J. Cryst. Growth*, 1999, **201**, 296, DOI: 10.1016/S0022-0248(98)01346-3.
8 S. Fernández-Garrido, G. Koblmüller, E. Calleja and J. S. Speck, *J. Appl. Phys.*, 2008, **104**, 1, DOI: 10.1063/1.2968442.
9 Z. Zhu, M. Hagino, K. Uesugi, S. Kamiyama, M. Fujimoto and T. Yao, *Jpn. J. Appl. Phys.*, 1989, **28**, 1659, DOI: 10.1143/JJAP.28.1659.
10 K. Kato, M. Sano, K. Miyamoto and T. Yao, *Jpn. J. Appl. Phys.*, 2003, **42**, 2241, DOI: 10.1143/JJAP.42.2241.
11 L. Pfeiffer, K. W. West, H. L. Stormer and K. W. Baldwin, *Appl. Phys. Lett.*, 1989, **55**, 1888, DOI: 10.1063/1.102162.
12 D. G. Schlom and L. N. Pfeiffer, *Nat. Mater.*, 2010, **9**, 881, DOI: 10.1038/nmat2888.
13 D. C. Tsui, H. L. Stormer and A. C. Gossard, *Phys. Rev. Lett.*, 1982, **48**, 1559, DOI: 10.1103/PhysRevLett.48.1559.
14 M. E. White, M. Y. Tsai, F. Wu and J. S. Speck, *J. Vac. Sci. Technol., A*, 2008, **26**, 1300, DOI: 10.1116/1.2966423.
15 M. Y. Tsai, O. Bierwagen, M. E. White and J. S. Speck, *J. Vac. Sci. Technol., A*, 2010, **28**, 354, DOI: 10.1116/1.3294715.
16 P. Vogt and O. Bierwagen, *Appl. Phys. Lett.*, 2015, **106**, 081910, DOI: 10.1063/1.4913447.
17 P. Vogt, A. Mauze, F. Wu, B. Bonef and J. S. Speck, *Appl. Phys. Express*, 2018, **11**, 115503, DOI: 10.7567/APEX.11.115503.
18 P. Vogt, F. V. E. Hensling, K. Azizie, J. P. McCandless, J. Park and K. DeLello, *et al.*, *Phys. Rev. Appl.*, 2022, **17**, 034021, DOI: 10.1103/PhysRevApplied.17.034021.
19 S. Raghuvansy, J. P. McCandless, M. Schowalter, A. Karg, M. Alonso-Orts and M. S. Williams, *et al.*, *APL Mater.*, 2023, **11**, 111113, DOI: 10.1063/5.0174373.
20 P. Vogt, F. V. E. Hensling, K. Azizie, C. S. Chang, D. Turner and J. Park, *et al.*, *APL Mater.*, 2021, **9**, 031101, DOI: 10.1063/5.0035469.
21 P. Vogt, D. G. Schlom, F. V. E. Hensling, K. Azizie, Z. K. Liu and B. J. Bocklund, *et al.*, *United States Patent.*, 2022, 11462402, https://patents.google.com/patent/US11462402B2/en.
22 N. Teraguchi, F. Kato, M. Konagai, K. Takahashi, Y. Nakamura and N. Otsuka, *Appl. Phys. Lett.*, 1991, **59**, 567, DOI: 10.1063/1.105388.
23 T. Okamoto, A. Yamada and M. Konagai, *J. Cryst. Growth*, 1997, **175**, 1045, DOI: 10.1016/S0022-0248(96)00984-0.
24 T. Shimada, F. S. Ohuchi, A. Koma and J. Jpn, *Appl. Phys.*, 1993, **32**, 1182, DOI: 10.1143/JJAP.32.1182.
25 G. Han, Z. G. Chen, J. Drennan and J. Zou, *Small*, 2014, **10**, 2747, DOI: 10.1002/smll.201400104.
26 N. Balakrishnan, E. D. Steer, E. F. Smith, Z. R. Kudrynskyi, Z. D. Kovalyuk and L. Eaves, *et al.*, *2D Mater.*, 2018, **5**, 035026, DOI: 10.1088/2053-1583/aac479.
27 J. B. Varley, J. R. Weber, A. Janotti and C. G. Van de Walle, *Appl. Phys. Lett.*, 2010, **97**, 142106, DOI: 10.1063/1.3499306.
28 J. B. Varley, H. Peelaers, A. Janotti and C. G. Van de Walle, *J. Phys.: Condens. Matter*, 2011, **23**, 334212, DOI: 10.1088/0953-8984/23/33/334212.
29 D. S. Liu, M. Hilse, A. R. Lupini, J. M. Redwing and R. Engel-Herbert, *ACS Appl. Nano Mater.*, 2023, **6**, 15029, DOI: 10.1021/acsanm.3c02602.
30 P. Vogt and O. Bierwagen, *Appl. Phys. Lett.*, 2016, **108**, 072101, DOI: 10.1063/1.4942002.
31 E. Ahmadi, O. S. Koksaldi, S. W. Kaun, O. Yuichi, D. B. Short and U. K. Mishra, *et al.*, *Appl. Phys. Express*, 2017, **10**, 041102, DOI: 10.7567/APEX.10.041102.
32 Y. Oshima, E. Ahmadi, S. Kaun, F. Wu and J. S. Speck, *Semicond. Sci. Technol.*, 2018, **33**, 015013.
33 P. Vogt and O. Bierwagen, *Phys. Rev. Mater.*, 2018, **2**, 120401(R), DOI: 10.1103/PhysRevMaterials.2.120401.
34 C. J. Frosch and C. D. Thurmond, *J. Phys. Chem.*, 1962, **66**, 877, DOI: 10.1021/j100811a027.
35 J. Valderrama-N and K. T. Jacob, *Thermochim. Acta*, 1977, **21**, 215, DOI: 10.1016/0040-6031(77)85019-3.
36 R. Colin, J. Drowart and G. Verhaegen, *Trans. Faraday Soc.*, 1965, **61**, 1364, DOI: 10.1039/TF9656101364.
37 P. Vogt, O. Brandt, H. Riechert, J. Lähnemann and O. Bierwagen, *Phys. Rev. Lett.*, 2017, **119**, 196001, DOI: 10.1103/PhysRevLett.119.196001.
38 K. M. Adkison, S. L. Shang, B. J. Bocklund, D. Klimm, D. G. Schlom and Z. K. Liu, *APL Mater.*, 2020, **8**, 081110.
39 P. Vogt, *Growth Kinetics, Thermodynamics, and Phase Formation of group-III and IV oxides during Molecular Beam Epitaxy*, Humboldt University of Berlin, 2017, DOI: 10.18452/18036.
40 L. N. Majer, T. Acartürk, P. A. Aken, W. Braun, L. Camuti and J. Eckl-Haese, *et al.*, *APL Mater.*, 2024, **12**, 091112, DOI: 10.1063/5.0224092.
41 S. Chae, H. Paik, N. M. Vu, E. Kioupakis and J. T. Heron, *Appl. Phys. Lett.*, 2020, **117**, 072105, DOI: 10.1063/5.0018031.
42 W. Chen, K. Egbo, H. Tornatzky, M. Ramsteiner, M. R. Wagner and O. Bierwagen, *APL Mater.*, 2023, **11**, 071110, DOI: 10.1063/5.0155869.
43 M. E. Davis and R. J. Davis, *Fundamentals of Chemical Reaction Engineering*, McGraw-Hili, 1221 Avenue of the Americas, New York, NY, 2003, 10020.
44 K. Sasak, A. Kuramata, T. Masui, E. G. Víllora, K. Shimamura and S. Yamakoshi, *Appl. Phys. Express*, 2012, **5**, 035502.
45 K. Azizie, F. V. E. Hensling, C. A. Gorsak, Y. Kim, N. A. Pieczulewski and D. M. Dryden, *et al.*, *APL Mater.*, 2023, **11**, 041102, DOI: 10.1063/5.0139622.
46 A. Mauze, Y. Zhang, T. Itoh, F. Wu and J. S. Speck, *APL Mater.*, 2020, **8**, 021104, DOI: 10.1063/1.5135930.
47 F. Liu, T. K. Truttmann, D. Lee, B. E. Matthews, I. Laraib and A. Janotti, *et al.*, *Commun. Mater.*, 2022, **3**, 69, DOI: 10.1038/s43246-022-00290-y.
48 Z. Wen, K. Khan, X. Zhai and E. Ahmadi, *Appl. Phys. Lett.*, 2023, **122**, 082101, DOI: 10.1063/5.0142107.

49 C. H. Ho, *ACS Omega*, 2020, **5**, 18527, DOI: **10.1021/acsomega.0c02623**.
50 Scientific Group Thermodata Europe (SGTE) Thermodynamic Properties of Inorganic Materials, in Lehrstuhl fuer Theoretische Huettenkunde (Ed), Landolt-Boernstein New Ser Gr IV, Springer, Verlag Berlin Heidelberg, 1999, vol. 19A.
51 J. O. Andersson, T. Helander, L. Hoglund, P. Shi and B. Sundman, Thermo-Calc DICTRA: computational tools for materials science, *Calphad*, 2002, **26**, 273.
52 M. Binnewies and E. Mielke, *Thermochemical Data of Elements and Compounds*, Wiley VCH, 2nd edn, 2002, DOI: **10.1002/9783527619818**.